OXFORD

Journal of Petrology, 2022, **63**, 1–16
https://doi.org/10.1093/petrology/egac092
Original Manuscript

Mixing Loops, Mixing Envelopes, and Scattered Correlations among Trace Elements and Isotope Ratios Produced by Mixing of Melts Derived from a Spatially and Lithologically Heterogenous Mantle

Yan Liang*

Department of Earth, Environmental and Planetary Sciences, Brown University, Providence, RI 02912, USA

*Corresponding author. Email: yan_liang@brown.edu

Abstract

Mixing has been widely used in the interpretation of radiogenic isotope ratios and highly incompatible trace element variations in basalts produced by melting of a heterogeneous mantle. The binary mixing model is constructed by considering mass balance of endmember components, which is independent of physical state and spatial distribution of the endmembers in the mantle source. Variations of radiogenic isotope ratios and highly incompatible trace elements in basalts also depend on the size and spatial distribution of chemical and lithological heterogeneities in the mantle source. Here we present a new mixing model and a mixing scheme that take into account of the size, spatial location, and melting history of enriched mantle (EM) and depleted mantle (DM) parcels in the melting column. We show how Sr, Nd, and Hf concentrations and isotope ratios in the aggregated or pooled melt collected at the top of the melting column vary as a function of location of the EM parcel in the melting column. With changing location of the EM parcel in the upwelling melting column, compositions of the pooled melt do not follow a single mixing curve expected by the binary mixing model. Instead, they define a mixing loop that has an enriched branch and a depleted branch joined by two extreme points in composition space. The origin of the mixing loop can be traced back to four types of EM distribution or configuration in the melting column. The shape of the mixing loop depends on the relative melting rate of the EM to that of the DM and the number and spacing of EM parcels in the melting column. Probabilities of sampling the enriched and depleted branches in the pooled melt are proportional to volume fractions of the enriched and depleted materials in the mantle source. Mixing of pooled melts from a bundle of melting columns results in mixing envelopes in the isotope ratio correlation diagrams. The mixing envelope is a useful tool for studying chemical variations in mantle-derived melts. As an application, we consider scattered correlations in $^{87}Sr/^{86}Sr$ vs. $^{143}Nd/^{144}Nd$ and $^{143}Nd/^{144}Nd$ vs. $^{176}Hf/^{177}Hf$ in mid-ocean ridge basalts. We show that such correlations arise naturally from melting of a spatially heterogeneous mantle.

Keywords: mantle heterogeneity, lithological heterogeneity, spatial distribution, fractional melting, binary mixing, mid-ocean ridge basalt, mixing loop, mixing envelope, isotope ratios

INTRODUCTION

Variations of radiogenic isotope and highly incompatible trace element ratios in basalts are generally attributed to mixing. In an isotope ratio correlation diagram, such as $^{87}Sr/^{86}Sr$ vs. $^{143}Nd/^{144}Nd$, magmas produced by mixing of melts derived from an enriched mantle (EM) source and a depleted mantle (DM) source define a hyperbola that connects isotope ratios of the enriched and depleted endmember compositions (e.g. Vollmer, 1976; Langmuir *et al.* 1978). The curvature of the hyperbola depends on the concentration ratio of the two endmembers. Given the proportion of enriched and depleted melts, the isotope composition of the well-mixed melt is uniquely determined and plotted as a point on the mixing hyperbola. The binary mixing model is constructed through mass balance and does not, however, consider the physical state and spatial distribution of the two endmember components in the mantle source. The geometry of the enriched component in the mantle source (i.e. its size, shape, and spatial distribution) exerts a strong influence on the variations of radiogenic isotope and highly incompatible trace element ratios in melts produced by melting of a spatially heterogeneous mantle (Richter & Daly, 1989; DePaolo, 1996; Liang, 2008, 2020; Liu & Liang, 2017, 2020; Bo *et al.*, 2018; Liang & Liu, 2018). This can be illustrated through the schematic diagram in Fig. 1 where five configurations of a two-component upwelling melting column consisting of 8% EM and 92% DM are shown.

In configuration (0), the EM is in the form of a long string (Fig. 1). Chemical and lithological signatures of EM and DM are sampled by melts at the top of the melting column concurrently. Mixing of melts derived from EM and DM in various proportions gives rise to a range of isotope ratios that fall on a hyperbola defined by the two endmember mantle sources. Although not explicitly stated in most geochemical studies (but see Koornneef *et al.*, 2012), the geometry of configuration (0) forms the basis for mixing calculations involving isotope or element ratios of melts derived from two mantle sources. The fraction of EM-derived melt is a free parameter in the mixing calculation. The mixed melt composition

Received: May 26, 2022. **Revised:** August 30, 2022. **Accepted:** September 5, 2022
© The Author(s) 2022. Published by Oxford University Press. All rights reserved. For permissions, please e-mail: journals.permissions@oup.com

Downloaded from https://academic.oup.com/petrology/article/63/9/egac092/6694267 by guest on 24 September 2022

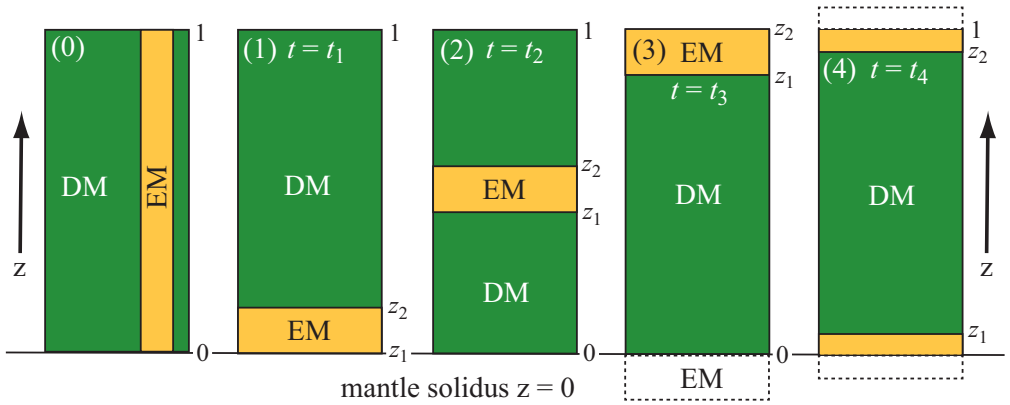

Figure 1. Schematic diagram showing five configurations of an EM parcel (colored in orange) in the background DM (green) in an upwelling melting column. The volume fractions of melt produced and EM in the mantle source are the same for the five cases, respectively. The mantle solidus is at the bottom of the melting column. The vertical coordinate is scaled by the height of the melting column so that $0 \le z \le 1$.

is independent of time and location of EM in the upwelling melting column.

In configurations (1)–(4), the EM has a finite size and is at different locations in the melting column (Fig. 1). The four configurations can be realized by considering an upwelling melting column in which pockets or blobs of EM are embedded in the background DM. The four configurations correspond to four times ($t = t_1$ to t_4) as a parcel of EM transits through the melting column. The EM parcel at the bottom of the melting column at time t_1 advects to the middle at time t_2 and the top of the melting column at time t_3 when a new EM layer is just about to enter the melting column from below. At time t_4, part of the EM parcel from configuration (3) has already exited the top of the melting column while part of the new EM parcel has just passed the solidus from below. In terms of their original volume fractions in the mantle source, the sum of the two EM parts in configuration (4) in the melting column is the same as in configurations (1)–(3). The EM parcel experiences the smallest extent of melting in configuration (1), intermediate extent of melting in configuration (2), and the highest extent of melting in configuration (3) as it transits through the melting column. The two smaller EM parcels in configuration (4) experience the lowest and the highest degrees of melting. Although Sr, Nd, and Hf isotope ratios of melts produced by melting of EM in the four configurations are the same, their elemental concentrations in the partial melts are different. If the composition or lithology of the EM source is different from the DM source, one would expect that Sr, Nd, and Hf isotope ratios of the pooled melts aggregated from EM and DM in each configuration will be different from each other and the reference configuration (0) in Fig. 1, even though the amount of melt produced in each case is the same. Hence, the mixed melt composition depends on time and spatial location of EM in the upwelling melting column.

The scenarios outlined in Fig. 1 are relevant to magma genesis beneath mid-ocean ridges and ocean islands where decompression melting of a spatially heterogeneous mantle gives rise to oceanic basalts that have a range of radiogenic isotope ratios and incompatible trace element concentrations. Models for trace element fractionation during decompression melting of a spatially distributed and chemically heterogeneous mantle have been discussed in several studies (e.g. DePaolo, 1996; Liang, 2008; Liu & Liang, 2017, 2020; Bo *et al.*, 2018; Liang & Liu, 2018). These models are applicable to cases where lithology and melting rate of the EM are the same as those of the DM. Rudge *et al.* (2013) presented a statistical model for 'mixing of fractional melts from a bi-lithological mantle source where small enriched fusible heterogeneities are embedded in a refractory depleted matrix'. However, the geometry of EM is not specified in their model. In a recent study, Liang (2020) presented a set of conservation equations for trace element fractionation during decompression melting of a spatially and lithologically heterogeneous mantle. As a first application, he obtained a simple analytical solution for perfect fractional melting of a two-lithology mantle in which melting rate of the enriched lithology is the same as that of the depleted lithology. The assumption of equal melting rate is necessary in order to obtain a simple analytical solution for the time-dependent problem. In general, different mantle lithologies have different melting rate. In this study, we consider one such case following the setup sketched in Fig. 1. Our chief objectives are (1) to integrate spatial distribution of mantle heterogeneity into geochemical mixing models and (2) to develop a better understanding of melting of a spatially and lithologically heterogeneous mantle.

The remainder of this paper is organized as follows. In the next two sections, we quantify the problem outlined in the preceding paragraph using a piecewise fractional melting model. We show variations of Sr, Nd, and Hf concentrations and isotope ratios in the pooled melt follow mixing loops and we trace their origin to the four configurations in Fig. 1. We then identify key factors affecting the shape of the mixing loop and variations of Sr, Nd, and Hf concentrations and isotope ratios in the pooled melt. We show that mixing of pooled melts from one or several mixing loops produces a mixing envelope in pairs of isotope ratio correlation diagrams. As an application, we consider scattered correlations in $^{87}Sr/^{86}Sr$ vs. $^{143}Nd/^{144}Nd$ and $^{143}Nd/^{144}Nd$ vs. $^{176}Hf/^{177}Hf$ in oceanic basalts. We suggest that such correlations arise naturally from aggregation of partial melts from a spatially heterogeneous mantle.

ONE-HETEROGENEITY MODEL

Compositions of the pooled melt in configurations (1)–(4) in Fig. 1 can be calculated using the time-dependent fractional or dynamic melting model with channelized melt extraction if the lithology or melting rate of EM is identical to that of DM (Liang, 2008, 2020; Liang & Liu, 2018). Here we consider a more general case in which lithologies and melting rates of EM and DM are not necessarily

Downloaded from https://academic.oup.com/petrology/article/63/9/egac092/6694267 by guest on 24 September 2022

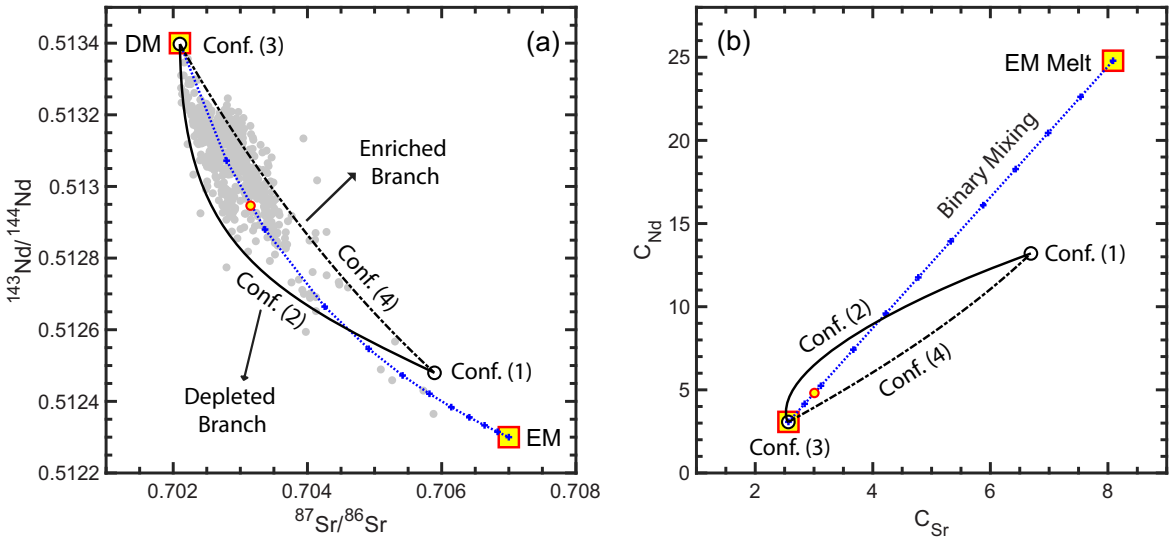

Figure 2. Covariations of Sr-Nd isotope ratios (a) and concentrations (b) in the pooled melt calculated using the one-heterogeneity model. The lithology of DM is spinel lherzolite (17% cpx + 27% opx + 53% olivine +3% spinel) and the lithology of EM is olivine websterite (7.5% cpx + 70% opx + 19.5% olivine +3% spinel). The volume fraction of EM in the mantle source is 8%. The extent of melting at the top of the melting column is 15% for both EM and DM. The dotted curves are binary mixing lines derived from mixing of pooled melts produced by 15% fractional melting of the pure DM and EM endmembers. The small yellow circle on the binary mixing curve marks the case of 8% of EM-derived melt. Small gray circles are MORB data from the Mid-Atlantic Ridge. Notations: Conf. (1), configuration (1); C_{Sr}, concentration of Sr in the pooled melt; C_{Nd}, concentration of Nd in the pooled melt.

the same. To make the analysis more tractable, we approximate the continuous process of decompression melting by a series of discrete time steps that span the four configurations in Fig. 1. We use the perfect fractional melting model to calculate concentrations of a trace element in instantaneous melts produced by melting of the EM and DM parcels while keeping track of their spatial locations in the melting column. We then aggregate all the fractional melts along the melting column to form the pooled melt at each time step. Because there is only one EM parcel at any time in the melting column, we call this case the one-heterogeneity model. Appendix A outlines the formulation of this model. Below we use a simple example to demonstrate the essential features of melting a spatially and lithologically heterogenous mantle. Cases with more than one heterogeneity in the melting column are presented in the next section.

Figure 2 presents an example of calculated Sr and Nd isotope ratios and elemental concentrations in the pooled melt for a case in which the melting rate of EM is the same as that of DM. For the purpose of illustration, we assume that the lithology of DM is spinel lherzolite and the lithology of EM is pyroxenite. In the Sr vs. Nd isotope ratio and concentration correlation diagrams, the pooled melts define mixing loops between two extreme points (open circles in Fig. 2). The most enriched point corresponds to configuration (1) and the most depleted point corresponds to configuration (3) in Fig. 1. As the EM layer advances through the melting column, starting from configuration (1), the pooled melt of configuration (2) becomes more and more depleted in terms of Sr and Nd concentrations and isotope ratios, defining a depleted branch in Fig. 2 (solid curves). By the time the EM layer reaches the upper part of the melting column, its Sr and Nd concentrations are so depleted by fractional melting that $^{87}Sr/^{86}Sr$ and $^{143}Nd/^{144}Nd$ of the pooled melt are dominated by isotopic signatures of the DM source. The endmember isotope composition of DM is recovered at configuration (3) in this example. (But this is not always the case, as will be demonstrated in Fig. 3 below.) As a new EM parcel passing through the bottom of the melting column (configuration (4)), Sr and Nd concentrations in the pooled melt increases, producing an enriched branch in the $^{87}Sr/^{86}Sr$ vs. $^{143}Nd/^{144}Nd$ diagram (dash-dotted curve in Fig. 2a). Because Sr is more incompatible than Nd, the enriched branch is plotted below the depleted branch in Fig. 2b. The end of configuration (4) corresponds to the most enriched point at configuration (1). Due to the small volume fraction of EM in the mantle source in this example (8%), the endmember isotope composition of EM is not recovered at configuration (1). Figure 2 also shows that the location of melts produced in configuration (1) is not on the binary mixing curve in the concentration and isotope ratio correlation diagrams. These are general features of melting a spatially heterogenous mantle, independent of EM lithology in the melting column. The mixing loop forms when compositions of EM- and DM-derived melts vary as a function of EM configuration or time in the melting column.

Figure 2 also compares the mixing loops with binary mixing curves that correspond to configuration (0) in Fig. 1. The extent of melting at the top of the melting column (15%) is the same among the five configurations. Mixing between the DM- and EM-derived melts of constant composition defines a straight line in the Sr vs. Nd correlation diagram and a hyperbola in the $^{87}Sr/^{86}Sr$ vs. $^{143}Nd/^{144}Nd$ correlation diagram (dotted blue lines in Fig. 2). All else being equal, configuration (0) produces a single pooled melt composition for a fixed EM-to-DM-derived melt ratio (8:92, small circles in Fig. 2), whereas configurations (1)–(4) produce a mixing loop for a fixed EM-to-DM ratio in the mantle source. At the time melts are sampled, the EM parcel in configurations (1)–(4) has experienced a different extent of melting in the melting column, which drives the concentrations of Sr and Nd in the pooled melt away from a single mixing line. This nonlinear mixing is stronger along the depleted branch than the enriched branch because Nd/Sr ratios are different between and vary along the two branches. Consequently, the mixing loop is asymmetric and rotates counterclockwise away from the binary mixing hyperbola in the $^{87}Sr/^{86}Sr$ vs. $^{143}Nd/^{144}Nd$ correlation diagram (Fig. 2a). Because of the large variations in Nd/Sr ratio, the depleted branch cannot be represented by a single mixing

Downloaded from https://academic.oup.com/petrology/article/63/9/egac092/6694267 by guest on 24 September 2022

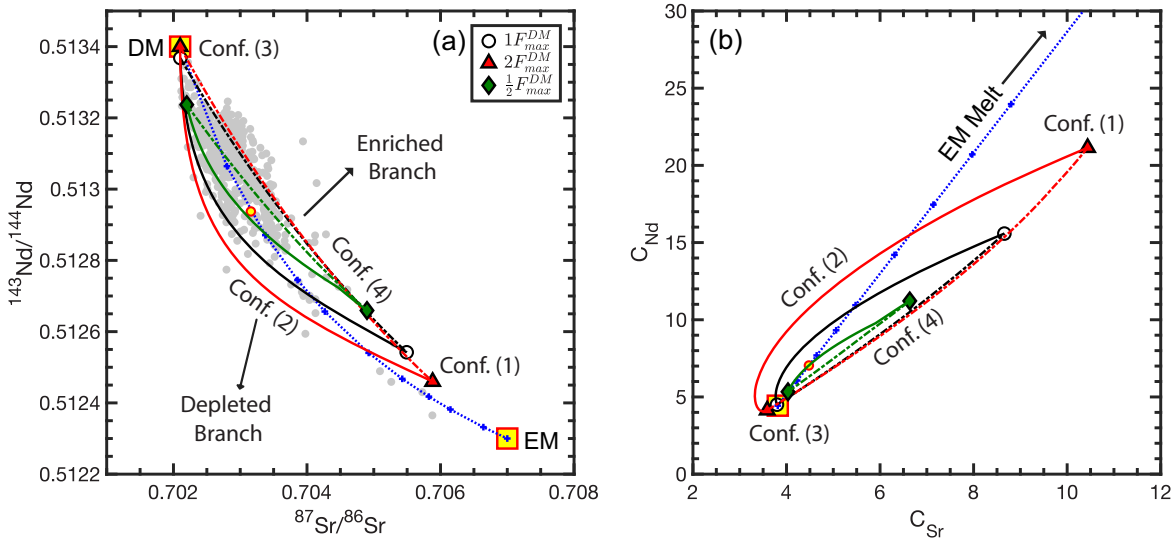

Figure 3. Similar to Fig. 2 but with the melting rate of EM 1, 2, and 1/2 times that of DM (black, red, and green curves, respectively). The maximum extent of melting of DM is 10%. Other melting parameters are the same as the case of equal melting rate shown in Fig. 2. The depleted branches and enriched branches are shown as the solid and dash-dotted lines and configurations (1) and (3) are identified by small open symbols in the two panels. The dotted curves are binary mixing lines derived from mixing of pooled melts produced by 10% fractional melting of the pure DM and EM endmembers. The small yellow circle on the binary mixing curve marks the case of 8% EM-derived melt.

hyperbola in the $^{87}Sr/^{86}Sr$ vs. $^{143}Nd/^{144}Nd$ correlation diagram even when melt compositions at configurations (1) and (3) are used as new endmembers. This is another general feature of melting a spatially heterogeneous mantle. If we pool all the melts produced in configurations (1)–(4), the time-integrated melt composition is plotted on the binary mixing curve as a single point (small yellow circles in Fig. 2a and b), recovering the case of configuration (0). This is a consequence of mass conservation (Liang, 2020).

The melting rates of EM and DM are the same in the preceding example. Figure 3 compares three cases in which the melting rates of EM are 1, 2, and 1/2 times of the melting rate of DM (black, red, and green curves, respectively). The maximum extent of melting experienced by DM at the top of the melting column is 10%. The maximum extent of melting experienced by EM is 10%, 20%, and 5%, respectively. Increasing EM-to-DM melting rate expands the mixing loop, whereas decreasing EM-to-DM melting rate shrinks the mixing loop in the isotope ratio correlation diagram. With increasing EM-to-DM melting rate, more EM-derived melt contributes to the pooled melt in configuration (1), driving its isotope composition closer to the pure EM endmember. However, a higher extent of melting of EM dilutes Sr and Nd concentrations in the pooled melt, which drives the isotope composition of the pooled melt at configuration (3) closer to the pure DM member (cf. circle and triangle near DM in Fig. 3a). Consequently, the mixing loop becomes longer and wider. With decreasing EM-to-DM melting rate, a smaller amount of EM-derived melt with higher Sr and Nd concentrations contributes to the pooled melt, resulting in less-depleted and less-enriched extreme values at configurations (3) and (1). The mixing loop becomes shorter and narrower. Figure 3b also shows an intriguing feature: Sr and Nd concentrations in the pooled melt in part of the depleted branch in the case of higher EM melting rate are lower than those in the pooled melt produced by melting of the pure DM endmember (large square). This is a dilution effect as higher degrees of fractional melting have effectively exhausted Sr and Nd in the residual pyroxenite.

MULTI-HETEROGENEITY MODEL

The geometry of the mixing loop also depends on the number of EM parcels in the melting column. The latter is determined by the volume fraction of EM and average distance between two adjacent EM layers (or the thickness of DM layer) in the mantle source. In the one-heterogeneity model, the distance between two adjacent EM layers is longer than the height of the melting column. With reducing distance between two adjacent EM layers there may be two or more EM parcels in the melting column. Here we consider a more general model in which there are N EM layers in configuration (1) in the melting column. For simplicity, we assume that the EM and DM layers are periodically distributed in the mantle source with constant thickness of h_0 and w_0, respectively. The volume fraction of EM in the mantle source feeding into the melting column is

$$\psi_0 = \frac{h_0}{h_0 + w_0}. \quad (1)$$

Supplementary Fig. S1 presents a schematic diagram showing the four configurations for a case in which there are three EM layers in the melting column. Appendix B provides a recipe for calculating spatial coordinates of EM and DM layers for configurations (1)–(4) in the melting column. Given the spatial coordinates, concentration of a trace element in the pooled fractional melt can be calculated through piecewise integrations across the alternating EM and DM layers in the melting column (Eqs. B9–B12).

Figure 4 compares variations of $^{87}Sr/^{86}Sr$, $^{143}Nd/^{144}Nd$, and $^{176}Hf/^{177}Hf$ in pooled melt for four cases in which there are 1, 2, 4, and 16 EM layers in the melting column and for two choices of EM-to-DM melting rate. For a constant EM volume fraction in the mantle source (8% in all cases here), the thickness and spacing of EM layers decrease with the number of EM parcels in the melting column. With increasing number of EM layers in the melting column, the mixing loop becomes shorter and narrower. Because Sr is more incompatible than Nd, which in turn is more incompatible than Hf, the mixing loop rotates

Downloaded from https://academic.oup.com/petrology/article/63/9/egac092/6694267 by guest on 24 September 2022

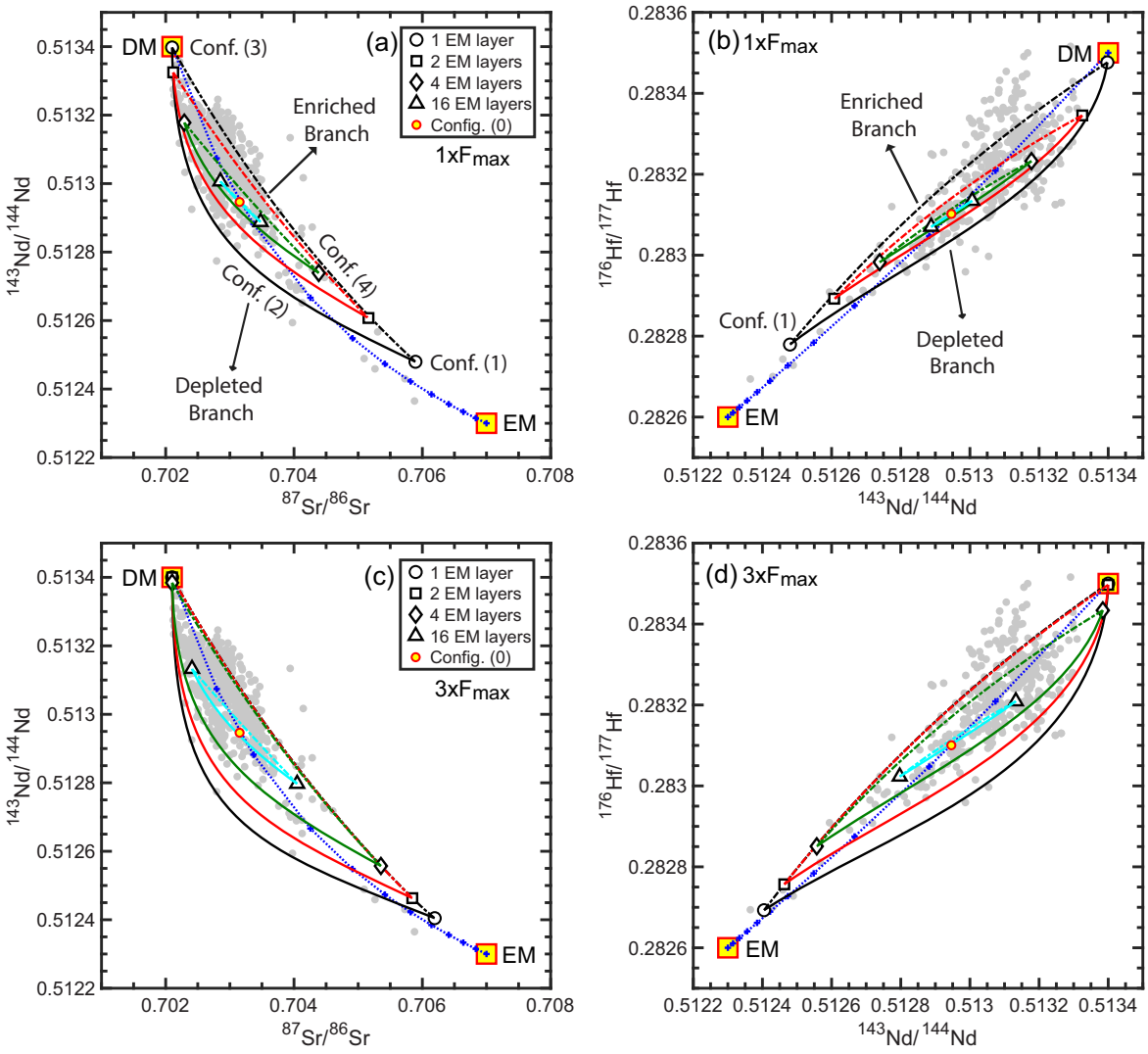

Figure 4. Similar to Fig. 2 but with three additional cases in which the number of EM layers in the melting column are 2 (red curves anchored by two squares), 4 (green curves anchored by two diamonds), and 16 (cyan curves anchored by two triangles). The depleted branches and enriched branches are shown as the solid and dash-dotted lines, respectively. Configurations (1) and (3) are identified by the open symbols. The volume fraction of EM is 8%. The melting rate of EM is the same as DM in panels (a) and (b), but three times that of DM in panels (c) and (d). The maximum extent of melting of DM is 15%. Figures showing variations in Sr, Nd, and Hf concentrations in the pooled melt are presented in supplementary Figs S2 and S3.

counterclockwise with respect to the binary mixing hyperbola in the $^{87}Sr/^{86}Sr$ vs. $^{143}Nd/^{144}Nd$ diagram (Fig. 4a and c) and clockwise in the $^{143}Nd/^{144}Nd$ vs. $^{176}Hf/^{177}Hf$ diagram (Fig. 4b and d). When the melting rate of EM is higher than that of DM, the mixing loop becomes longer and wider with the most-depleted and the most-enriched points shifting toward their respective pure endmembers (Fig. 4c and d). This is again a dilution effect, as higher degrees of fractional melting have effectively exhausted the incompatible trace elements in residual EM and DM.

Finally, we note that the number of samples in the enriched and depleted branches in the examples shown in Figs 2–4 are proportional to the amount of EM and DM in the mantle source. For example, if we sample 100 pooled melts at equal time increment through a complete DM-to-EM cycle, we have 92 samples from the depleted branch and 8 samples from the enriched branch. This is a general feature of fractional melting of a spatially heterogeneous mantle: the proportion of samples from the enriched and depleted branches are the same as the volume fractions of EM and DM in the mantle source when sampled randomly through a complete DM-to-EM cycle at equal time increment. However, this statement is valid only when mixing of the fractional melts is instantaneous at any given time during melt pooling. With finite melt mixing or aggregation time in the high-porosity channel or at the top of the melting column, we expect to sample more enriched melts when the melting rate of EM is higher than DM. Nonetheless, with less than 10% EM in the mantle source, the probability of sampling the enriched branch remains relatively small. This helps to explain the sparse tails toward the enriched endmember component in the MORB data shown in Fig. 4.

DISCUSSION

The preceding examples demonstrate the basic features of decompression melting of a spatially and lithologically heterogeneous mantle. To further understand the inner workings of melting a spatially heterogeneous mantle, we take a closer look at four physical parameters of the melting model: the size of EM parcel, the height of the melt column, the number of EM parcels, and the volume fraction of EM in the melting column. These physical parameters are essential for understanding the variations of

Downloaded from https://academic.oup.com/petrology/article/63/9/egac092/6694267 by guest on 24 September 2022

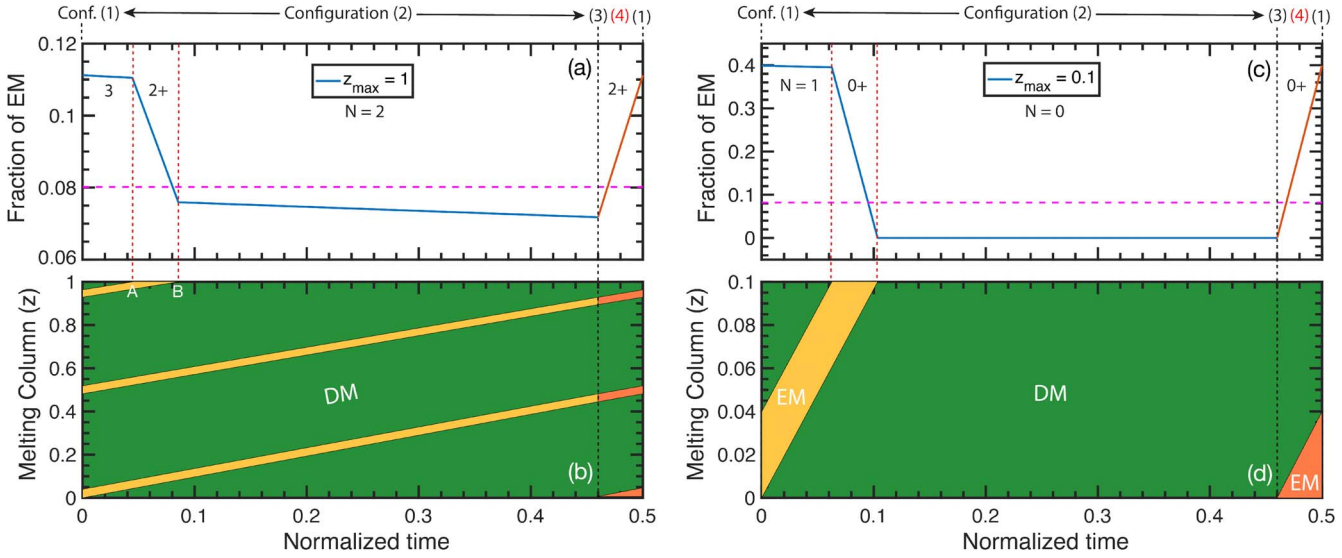

Figure 5. Variations of volume fraction of EM (a) and the number and thickness of EM layers (b) as a function of configuration or normalized time in the melting column ($0 \le z \le 1$). The volume fraction of EM in the mantle source is 8% (dashed horizontal line in (a)). There are two to three EM layers in the melting column (yellow and orange stripes, $h_0 = 0.04$ and $w_0 = 0.46$). The melting rate of EM is twice that of DM. The maximum extent of melting experienced by DM is 15% at $z = 1$. *N* is the number of EM layers in the melting column. The four configurations are identified at the top of panels (a) and (c). Dashed vertical lines mark the exit or entrance point of a lithological boundary. The depleted and enriched branches, which correspond to configurations (2) and (4), are separated by the long dashed vertical line at normalized time of 0.475 units. (c) and (d) are for a short melting column ($0 \le z \le 0.1$). The volume fraction, size and spacing of EM layers and melting rates of DM and EM are the same as the case shown in (a) and (b). For better visualization of EM layers in the melting column, a reader is referred to Supplementary Figs S4 and S5 for two cases in which the volume fraction of EM is 30%, the number of EM layers is four to five, and the EM:DM melting rates are 2 and 3, respectively.

isotope ratios and trace element concentrations in the pooled melt.

Variations of EM number and volume: the two extreme points of the mixing loop

Because of the finite size of each EM parcel, the number (*N*) and volume fraction of the sum of residual EM layers in the melting column (ψ, Eq. B7 in Appendix B) vary among the four configurations, even when the volume fraction of EM in the mantle source is constant over a length scale larger than the height of the melting column. Depending on EM-to-DM melting rate, the number of EM layers and the volume fraction of EM in the melting column fluctuate around reference values that are characteristic of the mantle source. These are illustrated in Fig. 5a and b for a case in which the number of EM layers varies from 2 to 3 in the melting column ($0 \le z \le 1$). The melting rate of EM is twice that of DM. The volume fraction of EM in the mantle source is 8%. From configurations (1) to (3), a new DM layer enters the melting column from below. The number of EM layers in the melting column decrease gradually from three to two (Fig. 5b). The volume fraction of residual EM layers in the melting column decreases from 11.2% at the point marked by configuration (1) in Fig. 5a to slightly below 11% at point A, then quickly down to 7.5% at point B when the top EM layer exits the melting column. Between point B and the point marked by configuration (3), the number of EM layers in the melting column is reduced to two and the volume fraction decreases slightly from 7.5% to 7.1% (Fig. 5b). This volume reduction is due to partial melting. The new DM layer in the lower half of the melting column completes its entrance at the point marked by configuration (3) where the volume fraction of residual EM is at its minimum. It is the combination of minimum EM volume fraction and the presence of a complete DM layer at the bottom of the melting column that gives rise to the most depleted point of the mixing loop shown in Figs 2–4. At configuration (3), a new EM layer starts its entrance from below. The volume fraction of residual EM increases as more EM enters the melting column from below. The end of configuration (4) is marked by the complete transit of the new EM layer through the bottom of the melting column. The system has three EM layers and returns to configuration (1) where the volume fraction of residual EM is at its maximum again (11.2%). This explains the origin of the most enriched point of the mixing loop at configuration (1): it arises from the combination of maximum EM volume fraction in the melting column and a new EM layer at the bottom of the melting column. Contributions of the enriched isotopic signal to the pooled melt are the highest at this extreme point. The nonlinear mixing curves in the C_{Sr} vs. C_{Nd} correlation diagram (Figs 2–3 and Fig. S2) are produced by the temporal variations in EM volume fraction and EM number in the melting column during decompression melting.

Relative size of EM parcels to the height of melting column: a magnifying effect

The actual height of the melting column also affects the geometry of the mixing loop. For a given EM size in the mantle source, the sizes of EM and DM layers relative to the height of the melting column increase when the height of the melting column decreases. This magnifying effect is illustrated in Fig. 5c and d for a short melting column ($0 \le z \le 0.1$). As the height decreases from 1 to 0.1, the number of EM layers in the melting column decreases from 3 to 1 in configuration (1), and the relative sizes of EM and DM layers in the melting column increase (cf. Fig. 5a and c). These lead to greater variations in EM volume fraction in the short melting column: from 40% in configuration (1) to 0% in a large part of configuration (2) and back to 40% in configuration (4) (Fig. 5c). When the size of DM layer is larger than the height of the melting column in part of configuration (2), the number and volume fraction of EM in the melting column reduce to zero

Downloaded from https://academic.oup.com/petrology/article/63/9/egac092/6694267 by guest on 24 September 2022

(Fig. 5c and d). It is possible then to sample pure DM and more enriched melts for the short melting column. Shorter melting columns therefore further expand the mixing loop, which has important implications for the interpretation of Sr-Nd-Hf isotope ratios in off-axis MORB samples (Liang, 2020; Liu & Liang, 2020). Despite the large temporal fluctuation in EM volume fraction, the average EM volume fraction for a complete cycle, i.e. from configurations (1) to (4), remains the same as the case of long melting column (dashed horizontal lines in Fig. 5a and c). This is a consequence of mass conservation.

Number of EM layers and EM melting rate: contraction of the mixing loop

For a given EM volume fraction in the mantle source, the difference between the maximum and minimum residual EM volume fraction decreases with the increase of EM layers (N) in the melting column. Doubling the number of EM layers ($N = 4 \sim 5$) in the example shown in Fig. 5a would bring the maximum and minimum EM volume fractions to 9.2% and 7.2%, respectively. (For $N = 8 \sim 9$, the maximum and minimum EM volume fractions are 8.3% and 7.3%, respectively.) In contrast, the relative difference between the maximum and minimum residual EM volume fractions increases with the increase of EM melting rate or the maximum extent of melting experienced by the EM parcel (Eq. A2). For example, increasing EM melting rate from two to three times the melting rate of DM would increase the relative maximum and minimum EM volume fraction difference from 22.7% to 25%. This helps to explain the expansion of mixing loops with decreasing N and increasing EM melting rate and the contraction of mixing loops with increasing N and decreasing EM melting rate (i.e. the trade-off in Fig. 4). With large enough N, the mixing loop eventually converges to a point on the binary mixing hyperbola, recovering the case of configuration (0) (small yellow circles in Fig. 4). However, the rate of convergence is slow with increasing N and EM melting rate. For example, with 128 EM layers in a 100-km melting column, the spacing between two adjacent EM layers is 780 m when there are 8% EM in the mantle source. The 'distance' or separation between the two extreme points of the mixing loop in the $^{87}Sr/^{86}Sr$ vs. $^{143}Nd/^{144}Nd$ diagram is reduced to 2%, 3.8%, and 7.4% of the distances when there is only one EM layer in the melting column and when the melting rate of EM is 1, 2, and 4 times of DM, respectively. Hence, some variations in radiogenic isotope ratios of Sr, Nd, and Hf in the pooled melt are expected during decompression melting of a spatially heterogenous mantle if the spacing between two adjacent EM layers is more than a few hundred meters. In supplementary Figs S6 and S7, we present examples that show the dependence of 'separation distance' on EM number and EM-to-DM melting rate.

MIXING ENVELOPES AND SCATTERED CORRELATIONS: AN APPLICATION

During decompression melting of a spatially heterogeneous two-component mantle, the simple binary mixing curve bifurcates into two branches, forming a mixing loop. With judicious selection of EM and DM composition, lithology, proportion, and size, it is possible to produce mixing loops that can enclose the observed Sr-Nd-Hf isotope ratios of basalts (cf. Figs. 2–4). In this section, we outline a mixing scheme that can fill in the composition space enclosed by the mixing loop. The filled in space defines a mixing envelope, which is useful for studying chemical variations in basalts.

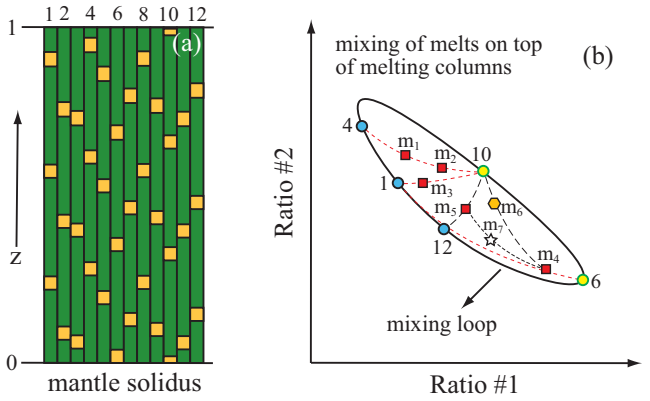

Figure 6. (a) Schematic diagram showing the bundles of column model for decompression melting of a spatially heterogeneous mantle in a rectangle melting region. (b) Isotope or elemental ratio correlation diagram illustrating the formation of the mixing envelope. The mixing envelope is defined by a collection of melts produced by mixing of pooled melts from the same mixing loop, remixing of mixed melts on top of the melting columns, and possibly points on the mixing loop. The EM parcels have the same geometry and periodicity in the mantel source for all the melting columns. Different melting columns have different EM configurations or spatial distributions. Pooled melts from these melting columns belong to the same mixing loop (points 1, 2, … 12).

Mixing envelope produced by mixing of melts from a mixing loop

The mixing model presented in the preceding sections is 1D, which implies a horizontally layered structure for EM and DM in 2D melting region. In general, the shape of EM parcel in the mantle source is unknown. Liu & Liang (2020) used circles of prescribed radii to model EM parcels in a 2D triangular melting region. Without loss of generality, we use rectangles to approximate the shape of EM parcel in the melting column. The width of the rectangle is the same as the width of the melting column. The 2D melting region is approximated by a bundle of vertically upwelling melting columns. Figure 6a presents an example in which EM parcels have the same width, height, and periodicity in the mantle source of the melting columns. The difference among the melting columns is the spatial distribution of EM parcels, which can be realized when EM parcels in different melting columns have different configurations (cf. Fig. 1). Hence, pooled melts from each of the melting columns in the 2D region are related to each other through the same mixing loop. This is illustrated in Fig. 6b. Depending on melt migration mechanism and geometry of the melting region, the pooled melt from one melting column may mix with the pooled melt from another melting column, forming a mixed melt on the top of the melting region. The mixed melt may mix again with a pooled column melt or another mixed melt, and these mixing processes may repeat several times. For example, mixing pooled melts from columns 4 and 10 in different proportions would produce mixed melts m_1 and m_2 in Fig. 6b, while mixing the mixed melt m_4 with the pooled melt from column 10 or the mixed melt m_5 would produce mixed melt m_6 or m_7. In a more general case when the relative size and/or number of EM parcels are different among the melting columns, several mixing loops are present (cf. Fig. 4). The pooled melts from different mixing loops may mix with each other on the top of the melting region. Collectively, these mixed and remixed melts would fill in the composition space enclosed by the mixing loops, forming a mixing envelope. The shape of the mixing envelope depends on the way different points on the mixing loop is mixed and remixed, i.e.

Downloaded from https://academic.oup.com/petrology/article/63/9/egac092/6694267 by guest on 24 September 2022

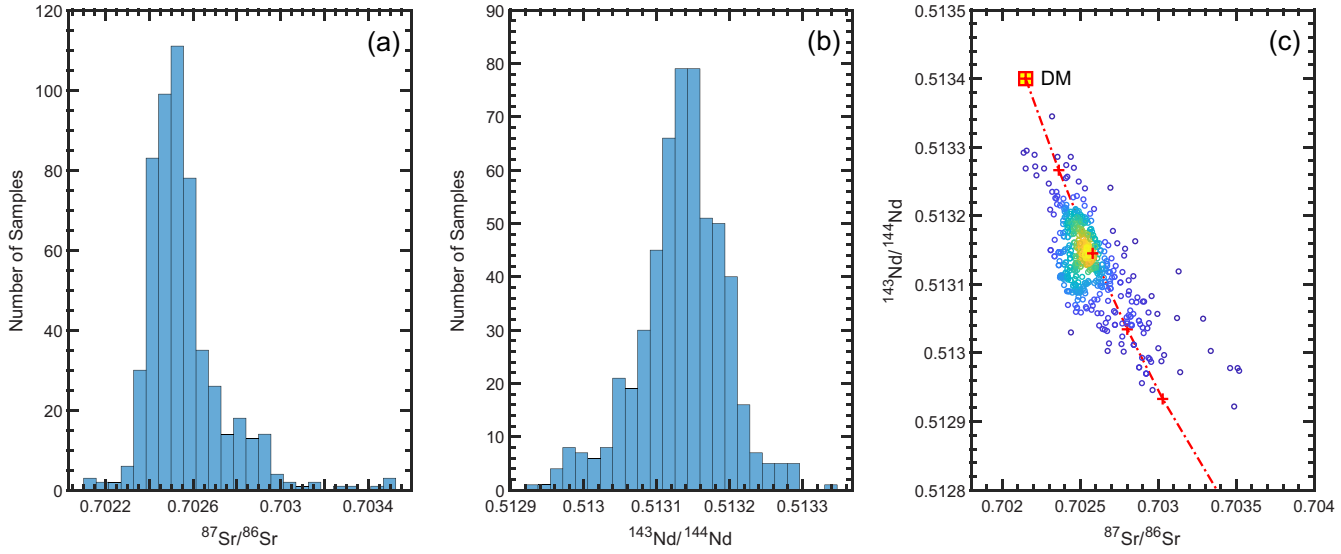

Figure 7. Histograms (a, b) and correlation diagram (c) showing Sr and Nd isotope ratios in 700 Pacific MORB samples. Small circles in (c) are data from Pacific MORB with sample density marked by blue (low) to yellow (high) colors. The red dashed curve is derived from mixing of DM and EM endmembers. The red plus symbols on the mixing curve mark the 5% increment of EM. Sources of data: compilation of Stracke (2012) from PetDB and Shimizu *et al.* (2016).

the mixing mechanism. In the next section, we outline a simple mixing scheme that is based on restacking and random sampling of the mixing loop. We show how the mixing envelope can be used to understand scattered correlations in Sr-Nd-Hf isotope ratio correlation diagrams in MORB samples.

Scattered correlations of Sr-Nd-Hf isotope ratios in Pacific MORB

Figure 7a and b are histograms showing the ranges and distributions of $^{87}Sr/^{86}Sr$ and $^{143}Nd/^{144}Nd$ in 700 Pacific MORB samples (data from Stracke, 2012; Shimizu *et al.*, 2016). About 200 data points are closely clustered around the bull's-eye centered at 0.7025 and 0.51314 in the $^{87}Sr/^{86}Sr$ vs. $^{143}Nd/^{144}Nd$ correlation diagram (Fig. 7c). The remaining 500 data have lower sample density and are more scattered: they extend toward the enriched and depleted components along the mixing curve, some above and some below (Fig. 7c). Collectively, the MORB trend defines a scattered correlation that has a high-density peak, a broad shoulder, and two sparse tails. Variations along the trend have generally been attributed to mixing involving a DM component and one or two EM components (e.g. Zindler *et al.*, 1984; Niu & Batiza, 1997; Niu *et al.*, 1999, 2002; Castillo *et al.*, 2000; Shimizu *et al.*, 2016; Mallick *et al.*, 2019). Possible explanations for the scatter of the MORB data include variations in mantle source composition and sampling of fractional melt from the melting region (e.g. Ito & Mahoney, 2005; Rudge *et al.*, 2013; Shimizu *et al.*, 2016; Liu & Liang, 2020; Stracke, 2021). During decompression melting of a spatially heterogeneous mantle, the EM number and volume fraction fluctuate around their mean values (Fig. 5), which may provide a simple explanation for the scattered correlation. Here we use a simple ridge model and the concept of mixing envelope to demonstrate this geometry effect.

Mid-ocean ridge basalts are aggregated melts produced by decompression melting over a broad region (e.g. Langmuir & Forsyth, 2007). Figure 8 presents a simplified treatment of melting a spatially heterogeneous mantle beneath the spreading center. It is similar to the bundles of column ridge model of Liu & Liang (2017, 2020) and Liang (2020) except the melting rates of EM and DM can now take on different values. Melts generated within each column are aggregated at the top of the melting column. These column-specific pooled melts are then funneled along high-porosity channels (not modeled here but see Sparks & Parmentier, 1991) toward the ridge axis and mixed in the axial magma chamber. Assuming instantaneous mixing in the magma chamber, the well-mixed melt (referred to as ridge melt hereafter) is the average of all the column-specific pooled melts weighted by their melt fluxes (Appendix C). Since the spatial distribution of EM parcels in the 2D cross-section at a given location on the ridge is generally different from the distribution at another location (e.g. the three cross sections in Fig. 8b), the ridge melt composition varies along the ridge.

The melting columns at a given distance away from the ridge axis in various cross-sections along the ridge have the same height but different EM configuration (e.g. column 9 in Fig. 8). Melt compositions from these equal height melting columns are part of the same mixing loop (cf. Fig. 6). Given the pooled melt compositions of a complete mixing loop for the melting column of height z_{max}, we construct an ensemble of pooled melts for the equal height melting columns by restacking the original data. Figure 9 presents a graphic illustration of restacking of a mixing loop that consists of 15 ordered data that span configurations (1)–(4), with entries or cells labeled as 1, 2, 3, . . . , 15. Each cell stores concentrations of trace element and isotope of interest in the pooled melt (e.g. ^{87}Sr, ^{86}Sr, REE, . . .) and the total melt flux (F_{top}, Eq. B8) at the top of the melting column at the given configuration or time during decompression melting. Starting from the original mixing loop, we randomly pick a point in the mixing loop as the new starting point (say cell 4 in Fig. 9). We obtain a restacked mixing loop (Stack #1 in Fig. 9) by moving the data points ahead of the selected point to the end of the mixing loop. We repeat the restacking for prescribed number of times (which equals to the number of cross sections in the ridge model) to obtain Stack #2, #3, . . . , #5. The restacked mixing loops are identical to the original mixing loop except each having a different starting cell (4, 14, 8, 2, and 12 in Fig. 9). Hence, these restacked mixing loops can be used to represent melting columns at a given location (x) in various

Downloaded from https://academic.oup.com/petrology/article/63/9/egac092/6694267 by guest on 24 September 2022

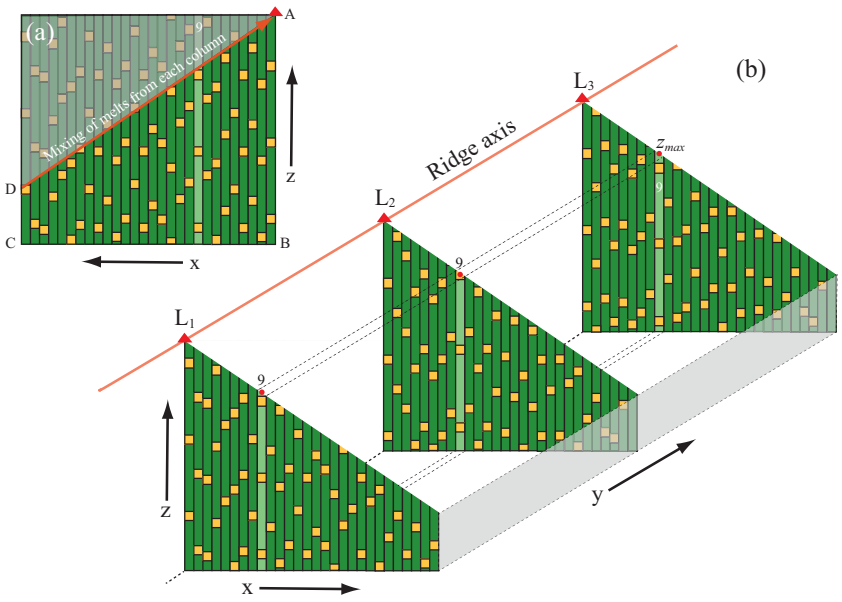

Figure 8. Schematic diagrams illustrating the setup of the bundles of column model for decompression melting of a spatially heterogeneous mantle beneath mid-ocean ridge spreading centers. (a) Melting region marked by ABCD. (b) Three cross-sections along the ridge axis. The size and spacing of EM parcels (yellow blocks), hence their volume fraction, in the mantle source are the same for each melting column. EM parcels in the four ridge cross sections have different spatial distribution but nearly the same volume fraction. Melts at the top of each melting column are funneled along a high-porosity channel toward the ridge axis and mixed in the axial magma chamber. The upper triangular region masked by gray shade in (a) is excluded in the modeling. It is shown to illustrate the spatial distribution of EM parcels in the melting columns. To aid discussion, DM in column 9 in the four cross-sections are shown in a different color. The size of EM (and DM) along the y direction is unspecified in this 2D model.

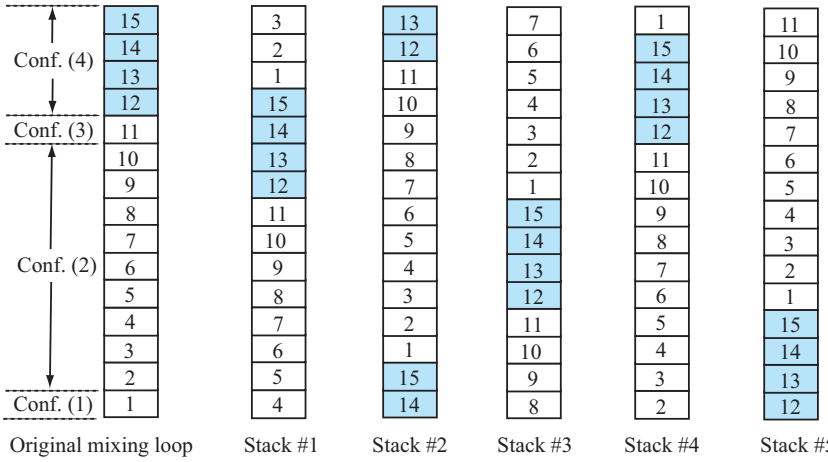

Figure 9. Graphic illustration of the restacking of a mixing loop. The original mixing loop consists of 15 ordered data that span configurations (1)–(4), with entries or cells labeled as 1, 2, 3,. . . , 15. Note that configurations (2) and (4) for the depleted and enriched branches have multiple entries. To create five mixing loops with new starting entries, we randomly draw five numbers between 1 and 15. The five numbers in the example presented here are 4, 14, 8, 2, and 12. We then move cells 1, 2, and 3 to the end of the original mixing loop to form Stack #1, cells 1–13 to the end of the original mixing loop to form Stack #2. We continue the restacking to form Stacks #3–5. Including the original mixing loop, the six Stacks form an ensemble of mixing loops that can be used to simulate spatial (from Stack to Stack at a given row) and temporal (from top to bottom for a given Stack) variations of trace elements and isotope ratios during decompression melting of a spatially and lithologically heterogenous mantle. If a mixing loop has M samples, there are a total of M possible combinations for the ensemble.

cross-sections along the ridge (e.g. column 9 in Fig. 8). To calculate ridge melt composition at a given location along the ridge, we randomly draw a pair of pooled melt composition and melt flux from each ensemble and take the weighted average across the ridge cross section using Eq. C1 in Appendix C. We repeat this step for prescribed number of times to form a collection of ridge melts that represent samples from different locations along the ridge (e.g. L_1, L_2 and L_3 in Fig. 8b).

Figure 10 compares Sr-Nd-Hf isotope ratios in the ridge melts with MORB data from the Pacific Ridge. To demonstrate the basic feature of the ridge model, we consider a two-lithology mantle source that consists of 8% olivine orthopyroxenite (2.5% cpx + 17.5% olivine +80% opx, EM) and 92% spinel lherzolite (17% cpx + 27% opx + 53% olivine +3% spinel, DM). The olivine orthopyroxenite can be produced by reaction between lherzolite and pyroxenite-derived melts (e.g. Yaxley & Green, 1998; Lo Cascio, 2008; Wang *et al.*, 2020). We assume that the melting rate of EM is twice that of DM. The melting region consists of 20 melting columns. The heights of the tallest and the shortest melting columns are 1 and 0.1 dimensionless units, respectively. Two cases

Downloaded from https://academic.oup.com/petrology/article/63/9/egac092/6694267 by guest on 24 September 2022

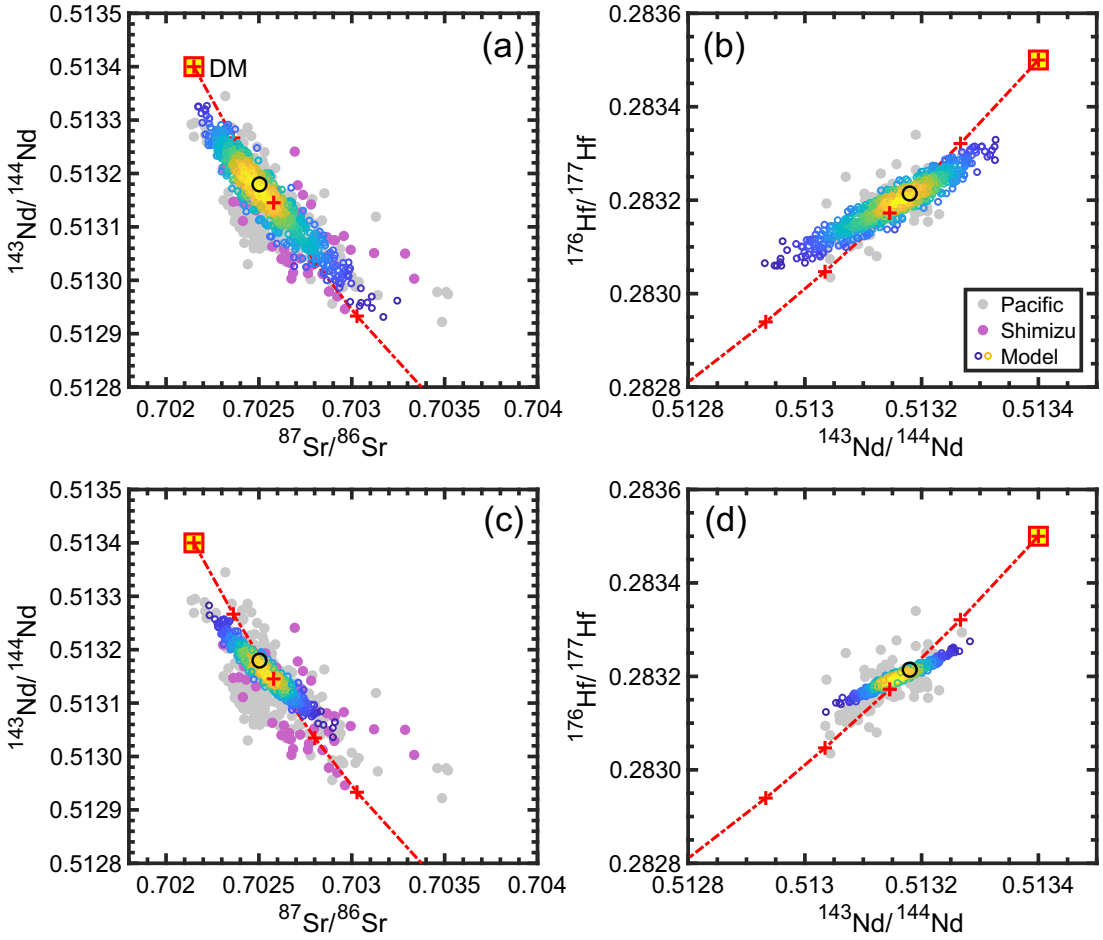

Figure 10. Scattered correlations of Sr-Nd-Hf isotope ratios in model-derived ridge melts produced by decompression melting of a two-lithology mantle (open circles). Sample density is mark by blue (low) to yellow (high) colors. There are three and eight EM parcels in the melting column directly beneath the ridge axis in the cases shown in panels (a, b) and (c, d), respectively. The lithology of DM is spinel lherzolite (17% cpx + 27% opx + 53% olivine +3% spinel) and the lithology of EM is an olivine orthopyroxenite (2.5% cpx + 80% opx + 17.5% olivine +3% spinel). The volume fraction of EM in the mantle source is 8%. The melting rate of EM is twice that of DM. The maximum extent of melting of DM is 15%. The dashed curves are binary mixing lines derived from mixing of DM and EM endmembers. The gray and purple circles are MORB data from the Pacific Ridge (Stracke, 2012; Shimizu *et al.*, 2016). The large black circle is the ridge melt for configuration (0) in Fig. 1. Model-derived Sr-Nd-Hf isotope data can be found in supplementary materials.

are shown: one with three EM parcels (Fig. 10a and b) and the other with eight EM parcels (Fig. 10c and d) in the melting column directly beneath the ridge axis. If melting starts 60 km beneath the ridge and the width of the melting region is 100 km, the sizes of EM parcels in the mantle source are 1.6×5 km^2 and 0.6×5 km^2 for the 3-heterogeneity and 8-heterogeneity ridge models, respectively.

If the distribution of EM within each melting column follows configuration (0) in Fig. 1 (i.e. in the form of long strings), the ridge melt compositions take on constant values and their isotope ratios are plotted very close to the 8% marker on the binary mixing curves in Fig. 10 (the large open circle in each panel). In the presence of spatially distributed EM parcels, the number and volume fraction of EM within each melting column fluctuate as a function of configuration and height of the melting column (Fig. 5). Consequently, a range of ridge melt compositions are produced. Figure 10 shows that ridge melts for each pair of isotope ratios define an elongated mixing envelope with sample densities peaked around the 8%–10% markers on the binary mixing curves (small orange to yellow circles). The two sparse tails are marked by small blue circles. The length of the sparse tail and the width of the mixing envelope depend on the number of EM parcels in the melting column and the EM-to-DM melting rate. For the lithologies and melting parameters considered, the 3-heterogeneity ridge model does a better job reproducing the first order features of the Pacific MORB than the 8-heterogeneity model. Histograms comparing results from the 3-heterogeneity model with the Pacific MORB data are provided in Supplementary Fig. S8.

There is a trade-off between the height and width of EM parcel in the bundles of column model (Liu & Liang, 2017, 2020). The width of each EM parcel, which is the same as the width of the melting column, equals the width of the melting region divided by the number of melting columns. Similar mixing envelopes could be obtained by judiciously choosing the number of EM parcels and the number of melting columns in the ridge model such that the area of the EM parcel remains the same. For example, variations and distributions of Sr-Nd-Hf isotope ratios from the case of 2-heterogeneity, 30-column ridge model are similar to the case of 3-heterogeneity, 20-column ridge model (Supplementary Figs S8–s10). Hence, the shape of EM parcel (in 2D and 3D) is also an important factor. In more complicated setups where mixing at the top of the high-porosity channel is incomplete or localized (see Fig. 4 in Liu & Liang, 2020) and the number and size of EM parcels in melting columns vary across the melting region, greater

Downloaded from https://academic.oup.com/petrology/article/63/9/egac092/6694267 by guest on 24 September 2022

variations in Sr-Nd-Hf isotope ratios are expected. These may help to explain at least some of the MORB data outside the mixing envelopes in Fig. 10.

SUMMARY AND FURTHER DISCUSSION

This study presents a new mixing model and a mixing scheme for trace element fractionation and isotope ratio variation during decompression melting of a heterogeneous mantle in which melting rates and sizes of the enriched and depleted lithologies are different. Mixing of melts derived from a spatially distributed two-lithology mantle is inherently nonlinear. The nonlinearity arises from the discrete nature of EM component in the melting column. Locations of EM pocket vary as a function of time during decompression melting. Consequently, the number and volume fraction of EM parcels in the melting column fluctuate around their mean values. This is in stark contrast with steady-state models in which the spatial distribution of EM in the melting column is independent of time. Instead of a single mixing line or hyperbola for a given pair of endmember compositions, mixing of melts derived from a spatially heterogeneous mantle results in mixing loops in concentration and isotope ratio correlation diagrams. The mixing loop consists of a depleted branch, an enriched branch, and two extreme points that correspond to the four configurations depicted in Fig. 1. In general, the enriched extreme point is not on the simple binary mixing curves defined by the two endmember components. Hence, caution should be exercised when using the most enriched isotope ratios in basalts to infer EM source compositions.

Key factors that determine the shape of the mixing loop in composition space include height of melting column, size of EM parcel, number of EM parcels in the melting column, relative EM-to-DM melting rate, as well as composition, lithology and proportion of the mantle component. The standard binary mixing model only considers the last three parameters. For a fixed EM composition, lithology, and volume fraction in the mantle source, we have the following general observations for decompression melting of a spatially heterogenous mantle:

(1) The size of EM parcel in the mantle source matters. With decreasing EM size, the number of EM parcels in the melting column increases for a constant EM volume fraction, the mixing loop becomes shorter and narrower and rotates away from the mixing curve defined by the binary mixing model. In the limit of very small EM size, hence large EM number, the mixing loop converges to a point on the binary mixing curve, recovering the binary mixing model.

(2) There is a trade-off between the number of EM parcels in the melting column and the relative EM-to-DM melting rate. The latter determines the relative extent of melting experienced by the two lithologies in the melting column. Increasing EM-to-DM melting rate expands the mixing loop, while decreasing EM-to-DM melting rate shrinks the mixing loop in the isotope ratio correlation diagram.

(3) All else being equal, larger variations in incompatible trace elements and radiogenic isotope ratios are expected for shorter melting column and larger EM size. It is the relative size of EM parcel to the height of the melting column that matters.

(4) Mixing of pooled melts from one or several mixing loops produces the mixing envelope in a pair of isotope ratio correlation diagram.

A ubiquitous feature of MORB samples from a given ocean basin is the scattered correlation in radiogenic isotope ratios (e.g. Zindler & Hart, 1986; Hofmann, 2014; Stracke, 2021). To understand this first-order observation, we develop a mixing scheme for the bundles of column ridge model. The ridge melt is a weighted average of pooled melts from all the melting columns in the 2D melting region. The weighing factor is the melt flux at the top of each melting column in the 2D melting region. This implies complete mixing of all fractional melts in the triangular melting region, an assumption that is also used in the steady-state ridge models (e.g. Holness & Richter, 1989; Plank & Langmuir, 1992; Plank *et al.*, 1995). A collection of ridge melts sampled along the ridge axis define the mixing envelope in a pair of isotope ratios correlation diagram.

The ridge melt composition varies as a function of upwelling time as different EM parcels entering and leaving the melting region at different times. Hence, the bundles of column ridge model can be used to study time series samples. However, there are far more chemical data for along-ridge MORB samples than across-ridge samples (but see Cordier *et al.*, 2010; Mougel *et al.*, 2021). The along-ridge samples can be regarded as random samples from a time series of pooled melts from a 2D cross-section if the spatial distributions of EM parcels within each 2D cross-sections along the ridge axis are statistically similar. This allows us to develop a mixing scheme for the bundles of column ridge model. Here we use mixing loop as a building block and construct an ensemble of pooled melts for melting columns of the same height along the direction of ridge axis through restacking of the mixing loop (Fig. 9). The assumptions for the restacking are as follows: (1) EM parcels have the same geometry and periodicity in the mantle source for each melting column; and (2) different along-strike melting columns have the same height but different EM configurations (e.g. column 9 in Fig. 8b). The latter implies that EM parcels are randomly distributed in the horizontal direction in the melting region. The imposed vertical periodicity for each melting column simplifies algebra and can be relaxed to more general cases.

Complete mixing over the entire melting region is an extreme endmember case. In a more likely scenario where mixing is incomplete or localized on the top of melting triangle, the mixing envelope becomes longer and broader. Liu & Liang (2020) provided several examples for Sr-Nd-Hf-Pb isotope ratios in locally aggregated or pooled melts produced by decompression melting of a spatially and chemically heterogeneous mantle in a melting triangle (see their Figs 4 and 10). Rudge *et al.* (2013) presented a statistical model for mixing of fractional melts from a two-lithology mantle. By sampling EM- and DM-derived fractional melts in different proportions through a prescribed statistical distribution, their model produces scattered correlations in isotope ratio correlation diagrams (Rudge *et al.*, 2013; Shimizu *et al.*, 2016). The main differences between their model and the ridge model from this study are the scheme of sampling fractional melts and the geometry and distribution of EM parcels in the melting region. The statistical model of Rudge *et al.* (2013) does not consider the size or geometry of EM parcels in the melting region, which hinders its application to time series samples. In theory, one can produce scattered correlations in Sr-Nd-Hf isotope ratio correlation diagrams by judiciously choosing a range of EM and DM compositions in the mantle source or/and by mixing of EM- and DM-derived melts in different proportions. The former implies a distribution of EM and DM compositions in the mantle source, whereas the latter requires a mixing scheme that depends on melt transport processes in the melting region, the decompaction boundary layer, and the crustal magma chamber. It is likely that both mantle source and melt migration processes

Downloaded from https://academic.oup.com/petrology/article/63/9/egac092/6694267 by guest on 24 September 2022

contribute to the scattered correlations in MORB samples. The present study highlights the importance of EM geometry and the relative EM-to-DM melting rate to variations of Sr-Nd-Hf isotope ratios in eruptible melts. More work is needed to quantify the mixing and sampling processes involved in the pooling of eruptible melts beneath the mid-ocean ridge (e.g. Sleep, 1984; Sparks & Parmentier, 1991; Phipps Morgan, 1999; Ito & Mahoney, 2005; Liang *et al.*, 2011; Katz & Weatherley, 2012; Koornneef *et al.*, 2012; Rudge *et al.*, 2013; Shimizu *et al.*, 2016; Liu & Liang, 2020; Stracke, 2021).

The lithology of EM in the source region of MORB is controversial and there are many types of pyroxenite (e.g. Hirschmann & Stolper, 1996; Kogiso *et al.*, 2004; Sobolev *et al.*, 2007; Lambart *et al.*, 2016; Matzen *et al.*, 2017). Changing clinopyroxene-to-orthopyroxene proportion in the pyroxenite changes the bulk solid-melt partition coefficients of Sr, Nd, and Hf in EM, resulting in contraction (increasing clinopyroxene mode) or expansion (decreasing clinopyroxene mode) of the mixing envelope. Supplementary Figs S11 and S12 present two examples—one for a clinopyroxene-free pyroxenite and the other for a pyroxenite with 10% clinopyroxene. Regardless of pyroxenite types, the presence of pyroxenite in the mantle source helps to explain the scatter of the MORB data. In the absence of lithological heterogeneity, the mixing envelope produced by melting of a chemically heterogenous mantle is significantly contracted (Supplementary Fig. S13). Hence, there is also a trade-off between lithology and composition of the EM component. Finally, for simplicity, we assume periodic distribution of EM parcels in the mantle source for each melting column. In a more general case, the spacing and size of EM parcels in the mantle source may not be uniform (i.e. vary along x or y direction in Fig. 8), which can affect details of ridge melt variation and may account for some of the mismatches between our model results and the Pacific MORB data. Regardless of the complications, Sr-Nd-Hf isotope ratios in the ridge melts exhibit scattered correlations. The scatter arises from spatial and temporal fluctuations in EM number and EM volume fraction in the melting region, which is an intrinsic feature of decompression melting of a spatially heterogeneous mantle.

ACKNOWLEDGMENTS

I thank Boda Liu for useful discussion and comments on an earlier version of the manuscript. Thoughtful reviews from John Rudge and two anonymous reviewers helped to improve the manuscript.

DATA AVAILABILITY STATEMENT

All the data underlying this manuscript are available in the manuscript and online supplementary material.

SUPPLEMENTARY DATA

Supplementary data are available at *Journal of Petrology* online.

FUNDING

This work was supported by National Science Foundation grant OCE-1852088.

References

Bo, T., Katz, R. F., Shorttle, O. & Rudge, J. F. (2018). The melting column as a filter of mantle trace-element heterogeneity. *Geochemistry, Geophysics, Geosystems* **19**, 4694–4721. https://doi.org/10.1029/2018GC007880.

Castillo, P. R., Klein, E., Bender, J., Langmuir, C., Shirey, S., Batiza, R. & White, W. (2000). Petrology and Sr, Nd, and Pb isotope geochemistry of mid-ocean ridge basalts from the 11°45'N to 15°00'N segment of the East Pacific Rise. *Geochemistry, Geophysics, Geosystems* **1**, 1011. https://doi.org/10.1029/1999GC000024.

Cordier, C., Benoit, M., Hémond, C., Dyment, J., Briais, A. & Kitazawa, M. (2010). Time scale of melt extraction revealed by distribution of lava composition across a ridge axis. *Geochemistry, Geophysics, Geosystems* **11**, Q0AC06. https://doi.org/10.1029/2010GC003074.

DePaolo, D. J. (1996). High-frequency isotopic variations in the Mauna Kea tholeiitic basalt sequence: melt zone dispersivity and chromatography. *Journal of Geophysical Research: Solid Earth* **101**, 11855–11864. https://doi.org/10.1029/95JB03494.

Hirschmann, M. M. & Stolper, E. M. (1996). A possible role for garnet pyroxenite in the origin of the "garnet signature" in MORB. *Contributions to Mineralogy and Petrology* **124**, 185–208. https://doi.org/10.1007/s004100050184.

Hofmann, A. W. (2014) Sampling mantle heterogeneity through oceanic basalts: isotopes and trace elements. In: Carlson R. W. (ed) *Treatise on Geochemistry: The Mantle and Core*, 2nd edn. New York: Elsevier, pp.67–101.

Holness, M. B. & Richter, F. M. (1989). Possible effects of spreading rate on MORB isotpic and rare earth composition arising from melting of a heterogeneous source. *The Journal of Geology* **97**, 247–260. https://doi.org/10.1086/629301.

Ito, G. & Mahoney, J. J. (2005). Flow and melting of a heterogeneous mantle: 1. Method and importance to the geochemistry of ocean island and mid-ocean ridge basalts. *Earth and Planetary Science Letters* **230**, 29–46. https://doi.org/10.1016/j.epsl.2004.10.035.

Katz, R. F. & Weatherley, S. M. (2012). Consequences of mantle heterogeneity for melt extraction at mid-ocean ridges. *Earth and Planetary Science Letters* **335-336**, 226–237. https://doi.org/10.1016/j.epsl.2012.04.042.

Kogiso, T., Hirschmann, M. M. & Pertermann, M. (2004). High-pressure partial melting of mafic lithologies in the mantle. *Journal of Petrology* **45**, 2407–2422. https://doi.org/10.1093/petrology/egh057.

Koornneef, J. M., Stracke, A., Meier, M. A., Jochum, K. P., Stoll, B. & Grönvold, K. (2012). Melting of a two-component source beneath Iceland. *Journal of Petrology* **53**, 127–157. https://doi.org/10.1093/petrology/egr059.

Lambart, S., Baker, M. B. & Stolper, E. M. (2016). The role of pyroxenite in basalt genesis: Melt-PX, a melting parameterization for mantle pyroxenites between 0.9 and 5 GPa. *Journal of Geophysical Research: Solid Earth* **121**, 5708–5735. https://doi.org/10.1002/2015JB012762.

Langmuir, C. H. & Forsyth, D. W. (2007). Mantle melting beneath mid-ocean ridges. *Oceanography* **20**, 78–89. https://doi.org/10.5670/oceanog.2007.82.

Langmuir, C. H., Vocke, R. D., Jr., Hanson, G. N. & Hart, S. R. (1978). A general mixing equation with applications to Icelandic basalts. *Earth and Planetary Science Letters* **37**, 380–392. https://doi.org/10.1016/0012-821X(78)90053-5.

Liang, Y. (2008). Simple models for dynamic melting in an upwelling heterogeneous mantle column: analytical solutions. *Geochimica et Cosmochimica Acta* **72**, 3804–3821. https://doi.org/10.1016/j.gca.2008.05.050.

Liang, Y. (2020). Trace element fractionation and isotope ratio variation during melting of a spatially distributed and lithologically heterogeneous mantle. *Earth and Planetary Science Letters* **552**, 116594. https://doi.org/10.1016/j.epsl.2020.116594.

Liang, Y. & Liu, B. (2018). Stretching chemical heterogeneity by melt migration in an upwelling mantle: an analysis

Downloaded from https://academic.oup.com/petrology/article/63/9/egac092/6694267 by guest on 24 September 2022

based on time-dependent batch melting and fractional melting models. *Earth and Planetary Science Letters* **498**, 275–287. https://doi.org/10.1016/j.epsl.2018.06.042.

Liang, Y., Schiemenz, A., Hesse, M. A. & Parmentier, E. M. (2011). Waves, channels, and the preservation of chemical heterogeneities during melt migration in the mantle. *Geophysical Research Letters* **38**. https://doi.org/10.1029/2011GL049034.

Liu, B. & Liang, Y. (2017). The prevalence of kilometer-scale heterogeneity in the source region of MORB upper mantle. *Science Advances* **3**, e1701872. https://doi.org/10.1126/sciadv.1701872.

Liu, B. & Liang, Y. (2020). Importance of the size and distribution of chemical heterogeneities in the mantle source to the variations of isotope ratios and trace element abundances in mid-ocean ridge basalts. *Geochimica et Cosmochimica Acta* **268**, 383–404. https://doi.org/10.1016/j.gca.2019.10.013.

Lo Cascio, M. (2008) Kinetics of partial melting and melt-rock reaction in the Earth's mantle. Ph.D. thesis, Brown University, https://doi.org/10.7301/Z0SF2TK0.

Mallick, S., Salters, V. J. M. & Langmuir, C. H. (2019). Geochemical variability along the northern East Pacific Rise: conincident source composition and ridge segmentation. *Geochemistry, Geophysics, Geosystems* **20**, 1889–1911. https://doi.org/10.1029/2019GC008287.

Matzen, A. K., Wood, B. J., Baker, M. B. & Stolper, E. M. (2017). The roles of pyroxenite and peridotite in the mantle sources of oceanic basalts. *Nature Geoscience* **10**, 530–535. https://doi.org/10.1038/NGEO2968.

Mougel, B., Agranier, A., Memond, C. & Gente, P. (2021). High-resolution isotopic variability across EPR segment 16°N: a chronological interpretation of source composition and ridge-seamount interaction. *Geochemistry, Geophysics, Geosystems* **22**, e2021GC009781. https://doi.org/10.1029/2021GC009781.

Niu, Y. & Batiza, R. (1997). Trace element evidence from seamounts for recylced oceanic crust in the Eastern Pacific mantle. *Earth and Planetary Science Letters* **148**, 471–483. https://doi.org/10.1016/S0012-821X(97)00048-4.

Niu, Y., Batiza, R., Wendt, J. I. & Regelous, M. (1999). Origin of enriched-type mid-ocean ridge basalt at ridges far from mantle plumes: the East Pacific Rise at 11°20'N. *Journal of Geophysical Research* **104**, 7067–7087. https://doi.org/10.1029/1998JB900037.

Niu, Y., Regelous, M., Wendt, I. J., Batiza, R. & O'Hara, M. J. (2002). Geochemistry of near-EPR seamounts: importance of source vs. process and the origin of enriched mantle component. *Earth and Planetary Science Letters* **199**, 327–345. https://doi.org/10.1016/S0012-821X(02)00591-5.

Phipps Morgan, J. (1999). Isotope topology of individual hotspot basalt arrays: mixing curves or melt extraction trajectories? *Geochemistry, Geohpysics Geosystems* **1**, 1003. https://doi.org/10.1029/1999GC000004.

Plank, T. & Langmuir, C. H. (1992). Effects of the melting regime on the composition of the oceanic crust. *Journal of Geophysical Research* **97**, 19749–19770. https://doi.org/10.1029/92JB01769.

Plank, T., Spiegelman, M., Langmuir, C. H. & Forsyth, D. W. (1995). The meaning of "mean F": clarifying the mean extent of melting at ocean ridges. *Journal of Geophysical Research* **100**, 15045–15052. https://doi.org/10.1029/95JB01148.

Richter, F. M. & Daly, S. F. (1989). Dynamical and chemical effects of melting a heterogeneous source. *Journal of Geophysical Research: Solid Earth* **94**, 12499–12510. https://doi.org/10.1029/JB094iB09p12499.

Rudge, J. F., Maclennan, J. & Stracke, S. (2013). The geochemical consequences of mixing melts from a heterogeneous mantle. *Geochimica et Cosmochimica Acta* **114**, 112–143. https://doi.org/10.1016/j.gca.2013.03.042.

Shaw, D. M. (1970). Trace element fractionation during anatexis. *Geochimica et Cosmochimica Acta* **34**, 237–243. https://doi.org/10.1016/0016-7037(70)90009-8.

Shimizu, K., Saal, A., Myers , C. E., Nagle, A. N., Hauri, E. H., Forsyth, D. W., Kamenetsky, V. S. & Niu, Y. (2016). Two-component mantle mixing model for the generation of mid-ocean ridge basalts: Implications for the volatile content of the Pacific upper mantle. *Geochimica et Cosmochimica Acta* **176**, 44–80. http://dx.doi.org/10.1016/j.gca.2015.10.033.

Sleep, N. H. (1984). Tapping of magmas from unbiquitous mantle heterogeneities: an alternative to mantle plumes? *Journal of Geophysical Research* **89**(10), 029–10041.

Sobolev, A. V., Hofmann, A. W., Kuzmin, D. V., Yaxley, G. M., Arndt, N. T., Chung, S. L., Danyushevsky, L. V., Elliott, T., Frey, F. A., Garcia, M. O., Gurenko, A. A., Kamenetsky, V. S., Kerr, A. C., Krivolutskaya, N. A., Matvienkov, V. V., Nikogosian, I. K., Rocholl, A., Sigurdsson, I. A., Sushchevskaya, N. M. & Teklay, M. (2007). The amount of recycled crust in sources of mantle derived melts. *Science* **316**, 412–417. https://doi.org/10.1126/science.1138113.

Sparks, D. W. & Parmentier, E. M. (1991). Melt extraction from the mantle beneath spreading centers. *Earth and Planetary \Science Letters* **105**, 368–377. https://doi.org/10.1016/0012-821X(91)90178-K.

Stracke, A. (2012). Earth's heterogeneous mantle: a product of convection-drive interaction between crust and mantle. *Chemical Geology* **330-331**, 274–299. https://doi.org/10.1016/j.chemgeo.2012.08.007.

Stracke, A. (2021). A process-oriented approach to mantle geochemistry. *Chemical Geology* **579**, 120350. https://doi.org/10.1016/j.chemgeo.2021.120350.

Vollmer, R. (1976). Rb-Sr and U-Th-Pb systematics of alkaline rocks: the alkaline rocks from Italy. *Geochimica et Cosmochimica Acta* **40**, 283–295. https://doi.org/10.1016/0016-7037(76)90205-2.

Wang, C., Lo Cascio, M., Liang, Y. & Xu, W. (2020). An experimental study of peridotite dissolution in eclogite-derived melts: implications for styles of melt-rock interaction in lithospheric mantle beneather the North China Craton. *Geochimica et Cosmochimica Acta* **278**, 157–176. https://doi.org/10.1016/j.gca.2019.09.022.

Workman, R. K. & Hart, S. R. (2005). Major and trace element composition of the depleted MORB mantle (DMM). *Earth and Planetary Science Letters* **231**, 53–72. https://doi.org/10.1016/j.epsl.2004.12.005.

Yaxley, G. M. & Green, D. H. (1998). Reactions between eclogite and peridotite: mantle refertilisation by subduction of oceanic crust. *Schweizerische Mineralogische und Petrographische Mitteilungen* **78**, 243–255.

Zindler, A. & Hart, S. (1986). Chemical geodynamics. *Annual Review of Earth and Planetary Sciences* **14**, 493–571. https://doi.org/10.1146/annurev.ea.14.050186.002425.

Zindler, A., Staudigel, H. & Batiza, R. (1984). Isotope and trace element geochemistry of young Pacific seamounts: implications for the scale of upper mantle heterogeneity. *Earth and Planetary Science Letters* **70**, 175–195. https://doi.org/10.1016/0012-821X(84)90004-9.

Appendix A. The One-Heterogeneity Model

Concentration of a trace element in the instantaneous melt produced by nonmodal perfect fractional melting (C_f) is given by

Downloaded from https://academic.oup.com/petrology/article/63/9/egac092/6694267 by guest on 24 September 2022

the familiar expression (Shaw, 1970):

$$C_f(F) = \frac{C_s^0}{k_s^0}\left(1 - \frac{k_s^p}{k_s^0}F\right)^{\frac{k_s^p - 1}{k_s^p}}, \quad \text{(A1)}$$

where C_s^0 is the mantle source composition (s = EM or DM); F is the degree of melting experienced by the mantle parcel as it upwells from the solidus to its current position in the melting column; and k_s^0 and k_s^p are bulk partition coefficients for the starting mantle and the melting reaction, respectively. For modal melting, we have $k_s^0 = k_s^p$. For a constant melting rate (Γ), the degree of melting of a mantle parcel (EM or DM) increases linearly upward in the melting column:

$$F = F_{max}z, F_{max} = \frac{\Gamma z_0}{\rho_s V_s^0}, \quad \text{(A2)}$$

where F_{max} is the maximum extent of melting experienced by the mantle parcel at the top of the melting column; and z is the dimensionless vertical coordinate, scaled by the height of the melting column (z_0). The top of the melting column is at z = 1 and the solidus is at z = 0. To simplify algebra, we assume that solidi of EM and DM are the same. For perfect fractional melting, this simplification has no effect on the pooled melt composition. Since F_{max} is proportional to melting rate, Eq. A2 is lithology specific.

If we aggregate all the melts generated between $z = z_a$ and $z = z_b$ in a lithologically homogeneous segment in the melting column (i.e. regions marked as DM or EM in Fig. 1), the amount of trace element in the locally pooled melt is given by the expression:

$$\begin{aligned} I(z_a, z_b) &= \frac{C_s^0}{k_s^0}\int_{z_a}^{z_b}\left(1 - \frac{k_s^p}{k_s^0}F_{max}x\right)^{\frac{k_s^p - 1}{k_s^p}} dx \\ &= \frac{C_s^0}{F_{max}}\left[\left(1 - \frac{k_s^p}{k_s^0}F_{max}z_a\right)^{\frac{1}{k_s^p}} - \left(1 - \frac{k_s^p}{k_s^0}F_{max}z_b\right)^{\frac{1}{k_s^p}}\right]. \end{aligned} \quad \text{(A3)}$$

The pooled melt at the top of the melting column is the weighted average of all the melts from the inter-stacked EM and DM layers in the melting column at a given time or configuration. For configurations (1)–(3) in Fig. 1, concentration of the trace element in the pooled melt derived from the inter-stacked DM-EM-DM layers is given by the expression:

$$C_f^{pool} = \frac{F_{max}^{DM} I_{DM}(0, z_1) + F_{max}^{EM} I_{EM}(z_1, z_2) + F_{max}^{DM} I_{DM}(z_2, 1)}{z_1 F_{max}^{DM} + (z_2 - z_1) F_{max}^{EM} + (1 - z_2) F_{max}^{DM}}, \quad \text{(A4)}$$

where subscripts or superscripts DM and EM refer to properties of the depleted and enriched mantle, respectively; z_1 and z_2 are location coordinates of the bottom and the top of the EM layer in the melting column (Fig. 1). The thickness of the EM layer in configurations (1)–(3) is $z_2 - z_1$. For configuration (4), we have the pooled melt concentration:

$$C_f^{pool} = \frac{F_{max}^{EM} I(0, z_1) + F_{max}^{DM} I(z_1, z_2) + F_{max}^{EM} I_{EM}(z_2, 1)}{z_1 F_{max}^{EM} + (z_2 - z_1) F_{max}^{DM} + (1 - z_2) F_{max}^{EM}}, \quad \text{(A5)}$$

where z_1 and z_2 are location coordinates of the bottom and the top of the DM layer in configuration (4). The denominators in Eqs. A4-A5 are the total fractions of melt produced in the heterogeneous melting column. They are the dimensionless melt fluxes. The partition coefficient and melting rate of EM are different from those of DM if the lithologies of EM and DM sources are different. Higher melting rate of EM contributes more melt to the pooled melt for a given EM volume fraction in the mantle source. Equations. A4-A5 represent a new mixing model that can be used to calculate trace element concentration in pooled melt produced by fractional melting of a spatially and lithologically heterogeneous mantle that has one enriched layer in the melting column.

To evaluate Eqs. A4-A5, we need to know the coordinates z_1 and z_2 in the melting column. In response to melting and melt extraction, the size of an EM parcel shrinks gradually as it moves upward through the melting column. For 50% fractional melting, the size of an EM parcel is half of its original size. Let h_0 be the original size or thickness of the EM layer in the mantle source relative to the height of the melting column. The thickness of the EM layer at location z in the melting column for configurations (1)–(3) can be estimated using an equation similar to that of Liang & Liu (2018, their Eq. 16a):

$$h(z) = z_2 - z_1 = \left[1 - \left(F_{max}^{DM} - F_{max}^{EM}\right) z_1 - F_{max}^{EM} z\right] h_0, \quad \text{(A6)}$$

where the second term in the bracket on the right-hand-side accounts for the difference in melting rate between DM and EM. Replacing z by the center of the EM layer, $z = (z_1 + z_2)/2$, we have

$$\left(1 + 0.5F_{max}^{EM}h_0\right) z_2 - \left[\left(1 - 0.5F_{max}^{EM}h_0\right) - \left(F_{max}^{DM} - F_{max}^{EM}\right) h_0\right] z_1 = h_0. \quad \text{(A7)}$$

To calculate pooled melt concentration using Eq. 4, we start from $z_1 = 0$ and use Eq. A7 to calculate z_2 (configuration (1)). We then march upward to a new z_1 (say $z_1 = 0.01$) and use Eq. A7 again to calculate a new z_2 (configuration (2)). This process is repeated until $z_2 = 1$, i.e. when configuration (3) is realized.

Location coordinates for configuration (4) are obtained as follows. Let f and $1 - f$ be the fractions of the enriched layer h_0 at the bottom and the top of the melting column. The thicknesses of the top and bottom EM layers are

$$1 - z_1 = \left(1 - F_{max}^{EM}\frac{1 + z_1}{2}\right) h_0 (1 - f), \quad \text{(A8)}$$

$$z_2 = \left(1 - F_{max}^{EM}\frac{z_2}{2}\right) h_0 f. \quad \text{(A9)}$$

Rearranging, we have the location coordinates for configuration (4):

$$z_1 = \frac{1 - \left(1 - 0.5F_{max}^{EM}\right) h_0 (1 - f)}{1 - 0.5F_{max}^{EM} h_0 (1 - f)}, \quad \text{(A10)}$$

$$z_2 = \frac{h_0 f}{1 + 0.5F_{max}^{EM} h_0 f}. \quad \text{(A11)}$$

Given the fraction of EM at the bottom of the melting column (f), the location coordinates for configuration (4) are calculated from Eqs. A10-A11 which are then used to calculate the pooled melt concentration from Eq. A5. This process can be repeated a number of times for $f = 0$ to 1.

Appendix B. The N-Heterogeneity Model

Here we consider a general case in which there are N to $N + 1$ EM layers in the melting column. This case is realized when

Downloaded from https://academic.oup.com/petrology/article/63/9/egac092/6694267 by guest on 24 September 2022

the center-to-center distance between two adjacent EM layers in the mantle source is between $1/N$ and $1/(N+1)$ of the height of the melting column. Supplementary Fig. S1 shows the four configurations for a 3-heterogeneity model. Let h_0 and w_0 be the thicknesses of the EM and DM layers in the mantle source. Their thicknesses at location z in the melting column can be estimated using the approach outlined in Appendix A. For configurations (1)–(3), we have a set of recursive equations for the spatial coordinates of EM layer j and its overlying DM layer:

$$\left(1+0.5F^{EM}_{max}h_0\right)z_{2j} - \left[\left(1-0.5F^{EM}_{max}h_0\right)z_{2j-1} - \left(F^{DM}_{max}-F^{EM}_{max}\right)h_0\sum_{k=1}^{2j-1}(-1)^{k-1}z_k\right] = h_0, \tag{B1}$$

$$\left(1+0.5F^{DM}_{max}w_0\right)z_{2j+1} - \left[\left(1-0.5F^{DM}_{max}w_0\right)z_{2j} - \left(F^{DM}_{max}-F^{EM}_{max}\right)w_0\sum_{k=1}^{2j}(-1)^{k-1}z_k\right] = w_0. \tag{B2}$$

To calculate the coordinates for configure (2), we start from Eq. B1 with $z_1=0$, which corresponds to configuration (1). We solve z_2 to z_{2j} or z_{2j+1} sequentially from Eqs. B1 and B2 for $j=1$ to $N+1$. We then increase z_1 by a small fraction and repeat the above steps. The maximum value for z_1 is

$$z_1 = \frac{w_0}{1+0.5F^{DM}_{max}w_0}, \tag{B3}$$

which is obtained by setting the thickness of the first EM layer in configuration (4) to zero (Eq. B5 below where indices for the top of EM layers are decreased by one for the convenience of coding; see Figure S1).

For configuration (4), the top of the first EM layer at the bottom of the melting column is z_1 (Fig. 1 and Fig. S1). We have the spatial coordinates

$$z_1 = \frac{h_0 f}{1+0.5F^{EM}_{max}h_0 f}, \tag{B4}$$

$$\left(1+0.5F^{DM}_{max}w_0\right)z_{2j} - \left[\left(1-0.5F^{DM}_{max}w_0\right)z_{2j-1} - \left(F^{EM}_{max}-F^{DM}_{max}\right)w_0\sum_{k=1}^{2j-1}(-1)^{k-1}z_k\right] = w_0, \tag{B5}$$

$$\left(1+0.5F^{EM}_{max}h_0\right)z_{2j+1} - \left[\left(1-0.5F^{EM}_{max}h_0\right)z_{2j} - \left(F^{EM}_{max}-F^{DM}_{max}\right)h_0\sum_{k=1}^{2j}(-1)^{k-1}z_k\right] = h_0, \tag{B6}$$

where f is the fraction of the enriched layer h_0 at the bottom of the melting column. To calculate the coordinates for configure (4), we start from Eq. B4 with $f=0$. We solve z_2 to z_{2j} or z_{2j+1} sequentially from Eqs. B5 and B6 for $j=1$ to $N+1$. We then increase f by a small fraction and repeat the above steps until $f=1$.

The volume fraction of residual EM in the melting column is the sum of all EM layers in the melting column:

$$\psi = \begin{cases} \sum_{j=1}^{N+1}\left(z_{2j}-z_{2j-1}\right) & \text{configurations (1)} - \text{(3)} \\ z_1+\sum_{j=1}^{N+1}\left(z_{2j+1}-z_{2j}\right) & \text{configuration (4)} \end{cases}. \tag{B7}$$

The fraction of melt extracted at the top of the heterogeneous melting column is the sum of melts derived from EM and DM layers in the melting column:

$$F_{top} = \begin{cases} F^{DM}_{max}z_1 + F^{EM}_{max}\sum_{j=1}^{N+1}\left(z_{2j}-z_{2j-1}\right) \\ \quad +F^{DM}_{max}\sum_{j=1}^{N+1}\left(z_{2j+1}-z_{2j}\right) & \text{configurations (1)} - \text{(3)} \\ F^{EM}_{max}z_1 + F^{DM}_{max}\sum_{j=1}^{N+1}\left(z_{2j}-z_{2j-1}\right) \\ \quad +F^{EM}_{max}\sum_{j=1}^{N+1}\left(z_{2j+1}-z_{2j}\right) & \text{configuration (4)} \end{cases}. \tag{B8}$$

The pooled melt is the weighted sum of all the melt produced in the melting column at a given time or configuration. For configurations (1)–(3), we can calculate the pooled melt concentration by a piece-wise integration, starting from the first DM layer at the bottom and going all the way to the top of the melting column (Figure S1):

$$C^{pool}_{f,1,2,3} = \frac{F^{DM}_{max}I_{DM}\left(0,z_1\right) + F^{EM}_{max}\sum_{j=1}^{N+1}I_{EM}\left(z_{2j-1},z_{2j}\right) + F^{DM}_{max}\sum_{j=1}^{N+1}I_{DM}\left(z_{2j},z_{2j+1}\right)}{F^{DM}_{max_{DM}}z_1 + F^{EM}_{max}\sum_{j=1}^{N+1}\left(z_{2j}-z_{2j-1}\right) + F^{DM}_{max}\sum_{j=1}^{N+1}\left(z_{2j+1}-z_{2j}\right)}. \tag{B9}$$

Similarly, for configuration (4), we have the pooled melt, starting from the first EM layer:

$$C^{pool}_{f,4} = \frac{F^{EM}_{max}I_{EM}\left(0,z_1\right) + F^{DM}_{max}\sum_{j=1}^{N+1}I_{DM}\left(z_{2j-1},z_{2j}\right) + F^{EM}_{max}\sum_{j=1}^{N+1}I_{EM}\left(z_{2j},z_{2j+1}\right)}{F^{EM}_{max}z_1 + F^{DM}_{max}\sum_{j=1}^{N+1}\left(z_{2j}-z_{2j-1}\right) + F^{EM}_{max}\sum_{j=1}^{N+1}\left(z_{2j+1}-z_{2j}\right)}. \tag{B10}$$

I_{EM} and I_{DM} are shorthand notations for the integrals of melt concentration across an EM or DM layer:

$$I_{EM}\left(z_a,z_b\right) = \frac{C^0_{EM}}{F^{EM}_{max}}\left[\left(1-\frac{k^p_{EM}}{k^0_{EM}}F^{EM}_{max}z_a\right)^{\frac{1}{k^p_{EM}}} - \left(1-\frac{k^p_{EM}}{k^0_{EM}}F^{EM}_{max}z_b\right)^{\frac{1}{k^p_{EM}}}\right], \tag{B11}$$

$$I_{DM}\left(z_a,z_b\right) = \frac{C^0_{DM}}{F^{DM}_{max}}\left[\left(1-\frac{k^p_{DM}}{k^0_{DM}}F^{DM}_{max}z_a\right)^{\frac{1}{k^p_{DM}}} - \left(1-\frac{k^p_{DM}}{k^0_{DM}}F^{DM}_{max}z_b\right)^{\frac{1}{k^p_{DM}}}\right], \tag{B12}$$

where the superscript or subscript EM and DM refer to property of EM and DM, respectively. Equations B9 and B10 are ensemble averages, i.e. they depend on spatial distributions of EM and DM in the melting column ($0\le z\le 1$). Since there are N to $N+1$ EM or DM layers in the melting column (Fig. 5), one has to set $z_{2j+1}=1$ or $z_{2j}=1$ if its value is great than one.

Downloaded from https://academic.oup.com/petrology/article/63/9/egac092/6694267 by guest on 24 September 2022

Appendix C. Ridge Melt Composition

Concentration of a trace element in the well-mixed ridge melt (C_f^{ridge}) is the weighted average of pooled melts collected from the top of all the melting columns in the bundles of column model. If a ridge cross section consists of *Nc* number of melting columns, we have *Nc* ensembles of pooled melts for columns 1, 2, …, *Nc* of decreasing height (Fig. 8b). To calculate ridge melt composition for a cross section, we draw pairs of melt flux and pooled melt composition from each ensemble and take the weighted average:

$$C_f^{ridge} = \frac{F_{top,1}C_{f,1}^{pool} + F_{top,2}C_{f,2}^{pool} + \ldots + F_{top,Nc}C_{f,Nc}^{pool}}{F_{top,1} + F_{top,2} + \ldots + F_{top,Nc}}, \qquad \text{(C1)}$$

where $F_{top,k}$ and $C_{f,k}^{pool}$ are the dimensionless melt flux and pooled melt concentration at the top of column *k* in the ridge model, respectively. $F_{top,k}$ and $C_{f,k}^{pool}$ can be calculated using Eqs. B8–B10 while keeping track of the height of the melting column. Note the melt flux also fluctuates because the number and thickness of EM layers in the melting column vary as a function of EM configuration during decompression melting (Eq. B8). Shorter melting column has smaller melt flux, and hence contributes less melt mass to the ridge melt.

Downloaded from https://academic.oup.com/petrology/article/63/9/egac092/6694267 by guest on 24 September 2022